ADVANCED MATERIALS
www.advmat.de

Atomistic Mechanisms Triggered by Joule Heating Effects in Metallic Cu-Bi Nanowires for Spintronics

*Alejandra Guedeja-Marrón, Juan Ignacio Beltrán, Matilde Saura-Múzquiz, Paolo Perna, M. Carmen Muñoz, Lucas Pérez, and Maria Varela**

Joule heating may severely impact the response to electric current injection of nanomaterials for spintronics. Here, the effects of heating in Bi doped Cu nanowires, a system where 1% Bi doping promotes a giant spin Hall effect (SHE), are studied by in situ high resolution electron microscopy. High quality Bi-Cu nanowires are grown by room temperature electrodeposition. The large size of Bi cations precludes insertion into the dense Cu face-centered lattice. Still, homogeneous compositions up to a nominal 7% Bi are successfully obtained with thicknesses <100 nm and grain sizes in the micron longitudinal scale, coated by a native oxide. In situ injection of current promotes fast Bi segregation out of solution. Controlled in situ annealing shows that the onset for segregation starts above temperatures of 250 °C. Within minutes, Bi atoms diffuse to grain boundaries or to exposed surfaces, such as the nanowire tips. Monoatomic thick Bi ordered decorations appear, preferentially on surface planes of the {320} type. Annealing at 400 °C promotes the growth of pure Bi nanocrystals, coherent with the underlying Cu matrix. Still, the intra-grain Bi concentration remains finite at values near 1%.
Density-functional theory calculations show that small amounts of Bi atoms are stable as substitutional impurities, confirming the potential of this system as building block for future spintronic devices.

1. Introduction

One of the main aims of the field of spintronics is the development of novel data storage technologies, for devices with faster operation speeds, reduced power consumption, or enhanced information density compared to conventional charge-based electronics.[1] Fundamental to these advances is the manipulation of spin degrees of freedom in nanostructured systems, where electrical current biasing is often employed to probe and control magnetic and spin-related phenomena such as spin-transfer torque, magnetoresistive switching or spin Hall effects.[2,3] However, the application of electrical currents inevitably leads to the generation of heat via the Joule effect.[4] The effects of such Joule heating can be particularly pronounced in nanoscale and low-dimensional systems, where limited heat dissipation pathways can result in a significant local temperature enhancement and give rise to unexpected phenomena.[5,6] Thermal gradients, temperature-dependent spin scattering, and thermally induced magnetic fluctuations can strongly influence spin current generation, propagation, and detection.[7] In devices operating under high current densities, Joule heating can alter key material parameters such as spin diffusion length, magnetic anisotropy, and even induce phase transitions that modify the device performance in unpredictable ways.[8] More importantly, heating can change the nanomaterial structure or chemical integrity itself in an irreversible fashion due to thermally activated mass diffusion or re-crystallization phenomena. Such processes may significantly affect the system magnetic response, for example, changing the coercivity of chemically intermixed interfaces in graphene-based magnetic heterostructures,[9] or modifying the capacitance of magnetic nanosystems.[10] Thus, a comprehensive understanding of heating phenomena is no longer a secondary consideration but an indispensable component for the reliable design, interpretation, and optimization of spintronic nanodevices.

However, harnessing such phenomena in nanomaterials demands a multidisciplinary approach, integrating material synthesis and advanced modeling with a careful experimental characterization at atomic resolution and with single atom sensitivity. While traditional *ex situ* methods often fail to capture

A. Guedeja-Marrón, J. Ignacio Beltrán, M. Varela
Dept. Física de Materiales & Instituto Pluridisciplinar
Universidad Complutense de Madrid
Madrid 28040, Spain
E-mail: mvarela@ucm.es

M. Saura-Múzquiz, L. Pérez
Dept. Física de Materiales
Universidad Complutense de Madrid
Madrid 28040, Spain

P. Perna
IMDEA Nanociencia
Madrid 28049, Spain

M. Carmen Muñoz
Instituto de Ciencia de Materiales de Madrid
Consejo Superior de Investigaciones Científicas
Madrid, Spain

The ORCID identification number(s) for the author(s) of this article can be found under https://doi.org/10.1002/adma.202513602

DOI: 10.1002/adma.202513602

the true behavior of materials under real-world operating conditions, in situ experiments combined with advanced characterization techniques, such as *in operando* spectroscopy,[11] X-ray or neutron diffraction,[12] or scanning transmission electron microscopy (STEM),[13] can recreate these conditions. In fact, in situ studies have become indispensable in modern materials science,[14] allowing real-time observation of dynamic changes in the structural and chemical state of materials subject to external stimuli, such as temperature, electric fields, or mechanical stress.[15–17] Within this context, high resolution in situ studies in the STEM enable direct monitoring of atomistic phenomena and critical processes in real space such as phase transitions, atomic diffusion, and strain-induced effects,[13,18–20] providing insights into how dynamic structural changes drive electronic, magnetic, and chemical properties of functional nanomaterials. Such insights become of fundamental importance when approaching metallic nanomaterials based on inhomogeneous systems or alloys where the physical functionality of interest emerges from doping a very dissimilar impurity into a densely packed matrix.

This is, indeed, the case for Cu-Bi alloys, a family where the very large Bi dopant is forced to sit into the Cu face-centered cubic (fcc) matrix lattice. This is a most interesting system for spintronics and spin charge conversion applications, since skew scattering caused by Bi dopants promotes a giant spin Hall effect (SHE), which increases with larger Bi content.[21–23] Therefore, this system represents a potential building brick for the next generation of spintronic devices. However, the large size of Bi ions immersed within the densely packed Cu fcc crystal lattice renders the solution unstable and particularly sensitive to heating effects, potentially preventing any practical implementation. In fact, macroscopically averaged in situ annealing studies based on variable temperature synchrotron powder X-ray diffraction (PXRD),[24] detect significant lattice changes along with nucleation of secondary phases upon heating, suggesting that Bi cations may be precipitating as metallic Bi clusters, thus lowering the intragrain Bi content responsible for optimal physical properties. The atomistic mechanisms underlying these phenomena are unclear and must be established if we are to harness this system. In fact, to this day it is not very clear whether Bi actually sits in solution as an impurity within the Cu fcc lattice, what doping levels may be stable, or which operation temperatures could be envisioned for devices including building blocks such as these. Any such thermally activated processes observed in Bi-doped Cu nanowires (NWs) may directly influence the SHE efficiency in this system.

Thus, it is necessary to understand both the structural features and the atomic-scale dynamics — particularly early-stage diffusion phenomena — of processes triggered by Joule heating, including migration pathways that may lead to secondary phase nucleation sites associated with Bi migration and clustering. Here, we present an in-depth in situ real space study with atomic resolution of the structural and chemical changes taking place in high quality, high Bi doping Cu nanowires subject to thermal excitation by means of high resolution electron microscopy and spectroscopy, along with first principles theoretical calculations. The combination of aberration corrected STEM and electron energy-loss spectroscopy (EELS) with the use of holders capable of applying external impulses such as heating or electric biasing in a controlled fashion provides a unique tool to analyze the local structural characteristics and thermal stability of such nanosystems in real space with high spatial resolution. Density-functional theory (DFT) will also be used as a tool to elucidate these processes and address fundamental questions about the structural stability and performance of these materials under future operational conditions.

2. Results

High quality Bi doped Cu NWs with Bi atomic contents up to 7% were grown by electrodeposition,[24] and they were subject to in situ electric biasing in the STEM in order to test their conducting properties and monitor any resulting phenomena. In situ biasing was carried out by applying a voltage to a collectivity of wires deposited by drop casting a solution rich in wires on a MEMS chip. **Figure 1a** presents a sketch, along with a low magnification image of a typical Wildfire-Lightning MEMS nanochip heater and electrical contact disposition, after deposition of the wires. A high amount of nanophase material randomly deposited on the MEMS chip is observed. The heater spiral (pink) and the four electrical contacts (straight leads) leading to the observation region, marked with a blue dashed rectangle, can be observed covered with a significant fraction of this NW (dark contrast) phase. Figure 1b displays an intermediate magnification view of a piece of material hanging between the electrical electrodes, with a single NW establishing contact from top to bottom. The wire was biased by applying a linear current ramp, from 5 to 19 μA, through the electrical pads of the holder. This net value reflects the nominal current flowing through the whole collectivity of nanophase material on the chip, so it is not possible to know the actual fraction circulating down this specific wire. As the current was increased, the average temperature on the chip membrane, measured by a thermocouple, was simultaneously monitored and observed to raise. It is worth highlighting that any increase in this macroscopically averaged temperature must result from heat transferred from the NW system carrying current to the macroscopic support, but it cannot in any way be assumed to reflect any specific single wire local temperature. In fact, the latter can be expected to be substantially higher due to the reduced cross-sectional area and localized heating effects. Following Holm´s classical treatment of thermal-electrical coupling in metallic constrictions, the relation: $V^2 = 4L(T^2 - T_0^2)$, where V is the voltage drop at the constriction, L is the Lorenz number and T and T_0 represent the temperatures of the constriction and its surroundings, respectively, can be used to relate voltage drops to local temperature.[25,26] Using the Lorenz number for copper ($L_0 = 2.44 \times 10^{-8}$ W Ω K^{-2}) and $T_0 = 300$ K, we can derive that a local voltage drop as low as ≈0.13 V would yield a constriction temperature of ≈250 °C (523 K), suggesting that this is the temperature range where Bi segregation is triggered. Figure 1c shows a set of high angle annular dark field (HAADF) intermediate magnification STEM images of the single NW as the nominal current through the system increases steadily, from left to right and from top to bottom, as marked on every frame. The images have been extracted from a video monitoring the whole measurement, which is included as video S1 in the supporting materials. Starting at 5 μA and 28 °C (top left panel) electric conduction along the NWs takes place, giving rise to power dissipation and Joule heating. The measured temperature rises at a

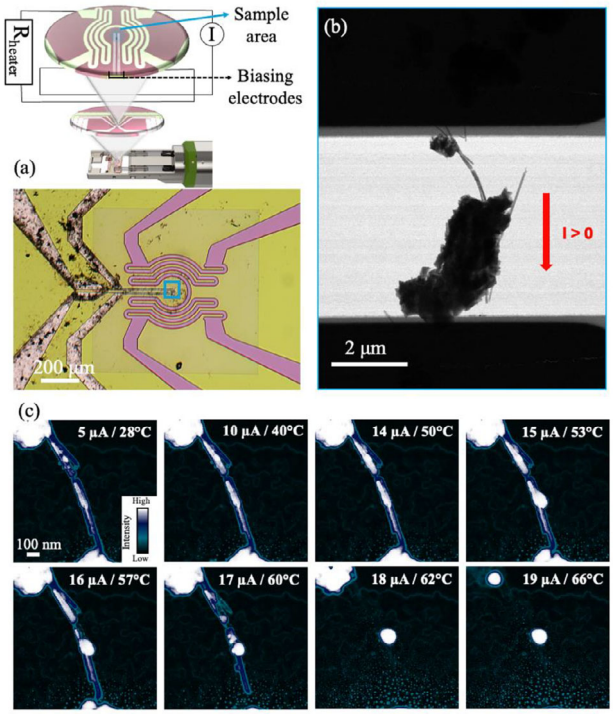

Figure 1. a) Schematic illustration of the Wildfire-Lightning nanochip (heating + biasing) set-up (top). It combines a four heater electrodes configuration: two electrodes for conducting a heating current and two others for measuring the generated voltage for calibration. Additionally, the nanochips are provided with four Pt electrodes for the injection of electrical stimuli. The sample area is highlighted in blue. Adapted from H. H. P. Garza et. al.[27] (Bottom) Optical view of the NW phase drop-casted onto the nanochip. The material deposited in between the electrodes is highlighted with a blue rectangle. b) Annular bright field (ABF) intermediate magnification image of a group of NWs resting in between the top and bottom electrodes to be used for electric polarization. A red arrow depicts the direction of electric intensity flow. c) HAADF-STEM images (in false color scale) acquired during the in situ current ramp with simultaneous tracking of the average temperature during a current injection in situ experiment performed on a Cu-Bi NW, with net intensity ranging from 5 to 19 µA, from left to right and from top to bottom (images extracted from video S1). Note that after the NW melts, the temperature keeps increasing due to a continued Joule effect associated with electric current flow continuing down the collectivity of other wires on the chip.

rate significantly higher than the current slope, reaching more than 60 °C by 19 µA. This is a hint of significant dissipation processes occurring through the NW system, which is not surprising since the dissipation power - and therefore, the temperature - should scale with the current intensity squared, I^2. Heating induced changes can be inferred from observation of the images. Being Bi a very heavy dopant, and since the contrast in HAADF images is roughly proportional to the atomic number squared, any compositional changes related to Bi segregation should be easily observed. While the HAADF contrast stays steady up to nominal current values near 10 µA, structural changes are triggered near 15 µA, with clear evidence of material migration in the form of a secondary nanometric phase appearing in the middle portion of the wire. The contrast associated with this phase is brighter than that of the Cu wire, suggesting that the average atomic number of the segregated material should be higher than that of Cu. Very likely, heavy Bi species are segregating out of solution, excited by the thermal energy in the system. As further current is injected, enough thermal energy is dissipated and the whole Cu wire is finally melted, by approximately nominal 18 µA, which approximately corresponds to a current density of $9{\cdot}10^5$ $A{\cdot}cm^{-2}$, if we assume that all of the current applied is flowing down this wire. Since we know this is not the case, this figure merely represents an upper estimation. We can conclude that Joule heating produces first an inhomogeneous segregation of heavy species (Bi), followed by a final melting of the whole NW. Similar processes taking place within a potential future device would compromise performance and, ultimately, become catastrophic. In order to understand and be able to avoid such phenomena in the future, an in-depth investigation of the thermally activated processes associated with heating is needed.

In order to study in detail any phenomena associated with heating, a set of pristine (as grown) wires with a nominal Bi content of 7% was subject to a controlled thermal annealing process in situ. The thermal treatment consisted of warming up the sample from room temperature (RT) to 400 °C at a rate of 3.74 °C s^{-1}, followed by quenching back to RT (after 15 min of thermal stabilization at 400 °C). **Figure 2** depicts a set of low magnification HAADF images showing the evolution of a single representative NW during the annealing (the whole process is depicted in video S2, in the supporting materials). Before annealing, at RT (Figure 2a), the wire exhibits a relatively uniform contrast excluding the presence of major secondary phases and pointing toward a homogeneous distribution of the Bi species within regions of hundreds of nm along the NW core axis. Minor inhomogeneities or defects are observed, such as the grain boundary highlighted in the blue rectangle at the bottom end. As the temperature is increased to 250–300 °C, noticeable changes are detected at the tips of the NW, and also near some of those defects – see for example the area marked with the blue square in Figure 2b. Regions with darker contrast appear, hinting to voids and pores in the previously solid NW, indicating the onset of mass diffusion and segregation processes. Additionally, regions looking like a few brighter nanoprecipitates (looking like bubbles, marked with red arrows) become visible as the temperature rises, highlighting the activation of segregation processes of heavy chemical species. Such bright nanoprecipitates become even more pronounced as the temperature keeps raising all the way up to 400 °C, as highlighted again with red arrows in Figure 2c. After reaching 400 °C, and keeping the temperature stable for 15 min, the HAADF signal from the NW core exhibits a much brighter contrast. Taking into account that Bi may be migrating out of solution, this observation must be explained from the analysis of the crystal structure. Indeed, a denser lattice would also explain this enhanced brightness, and a contraction of the material phase within the NW core is actually observed. The analysis of the lattice high resolution images in Figure 2d, acquired before and after annealing, throws a decreased later parameter of the Cu core, evolving from average values of (3.69 ± 0.05) down to (3.65 ± 0.05) Å. These values are consistent with our recent study, where macroscopically averaged lattice parameters were accurately determined via Rietveld analysis of synchrotron PXRD data. There, a contraction of the Cu lattice, from 3.6397(1) Å to 3.61887(4) was detected after a similar annealing process.[24] This ≈1% lattice parameter variation, associated with the core material contraction, explains the

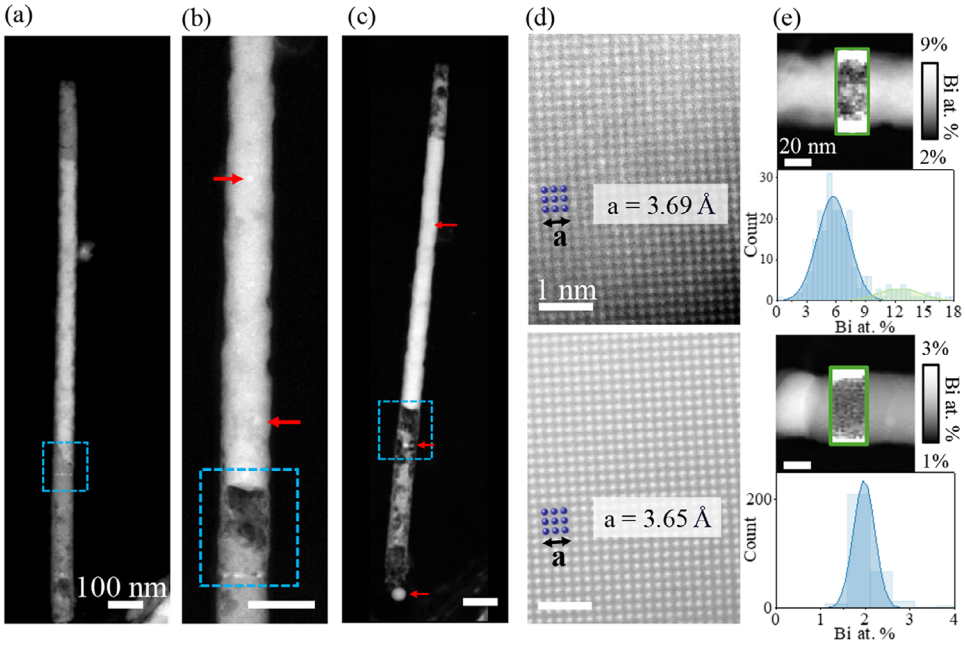

Figure 2. Left: HAADF-STEM images measured during an in situ heating experiment, with the complete time sequence shown in video S2. a) Starting point: pristine nanowire at RT. A blue rectangle marks the position of a defect near the NW bottom tip. b) Image acquired at a temperature near 300 °C, exhibiting significant segregation and formation of voids near the tip, along with a contraction of the NW core, already noticeable near the defect area (blue rectangle). Red arrows point to regions where some Bi segregation appears to take place in the form of nanoprecipitates. c) View of the nanowire at 400 °C. Red arrows point at Bi rich nanoprecipitates, while the blue rectangle highlights the same defect region as in (a,b). The inner core metallic Cu phase presents a bright contrast, while an inhomogeneous oxide phase at the shell remains after the annealing.[24] Scale bars in a-c represent 100 nm. d): HAADF-STEM atomic resolution images showing the unit cell down the [100] projection before (top) and after (bottom) annealing, with an overlaid sketch of the Cu fcc structure. The values of the cubic lattice constants obtained from these images are also labeled. The values were obtained from distribution of lattice distance values measured on the images after quantification of the locations of the atomic columns ´centers of mass, with error bars in the ±0.05 Å range, (determined by the standard deviation). Scale bars are 1 nm. e) HAADF images across the wires, before (top) and after (bottom) annealing at 400 °C. Scale bars represent 20 nm. The insets within green rectangles show the Bi relative composition, in atomic %, as measured from EEL spectrum images on those areas. The histograms below each image relate to the Bi atomic% composition from those EELS maps. Blue Gaussian fits refer to the major Bi phase, within the NW core, while the green Gaussian fit relates to Bi in the oxide shell. Contrast of the EELS maps has been manually adjusted based on the histogram fitting results to highlight the contribution of Bi within the grains.

higher HAADF contrast after annealing. The question of what is the effect of the annealing on Bi species remains open, though. The inhomogeneous contrast observed in the form of bright bubbles is likely associated with migration and clustering of the heavier element Bi. It is expected that high temperatures would also anneal other point defects likely generated during electrodeposition (such as Cu vacancies,[28,29] or other possible impurities such as H) promoting a lattice parameter reduction to values closer to those of fcc Cu, as observed.

Changes in Bi local composition and local Bi/Cu atomic ratios giving rise to inhomogeneities can be measured by EELS by quantifying the integrated signals from the Cu $L_{2,3}$ and Bi $M_{4,5}$ edges, with onsets near 931 and 2580 eV, respectively. The insets in green rectangles on the HAADF images shown in Figure 2e exhibit quantitative compositional Bi maps derived from EEL spectrum images, using the fitting routines available in the Digital Micrograph software,[30,31] measured across the nanowires on the pristine sample (top) and after the annealing at 400 °C (bottom). For each map, the bottom panels display the histograms associated with the quantitative local values of the Bi content. For the pristine sample, the compositional maps show that Bi is evenly distributed within the grains with a relative atomic percentage of (5.5 ± 1.6) % as measured from a Gaussian fit (in blue), which is in good agreement with the nominal content of 7%. The shell oxide layer shows a significant enrichment in Bi (near 12% according to the green Gaussian fit on the histogram), which should not affect the discussion of the core properties. Interestingly, upon quenching, the percentage of intra-grain Bi is significantly reduced to values in the average 1–2% range, according to the EELS map histogram in Figure 2e (bottom). This finding proofs that Bi species are, indeed, migrating out of solution due to the thermal effects. It is worth noting that annealing at higher temperatures did not produce any further Bi segregation, pointing toward the fact that low Bi concentrations of the order of 1–2% may be stable in solution. Since these could still give rise to the phenomena ensuing in a noticeable SHE over a large range of device operation temperatures, the stability of Bi into the Cu fcc lattice must be confirmed.

For this aim, we resorted to first principles calculations, using DFT to investigate the stability of Bi defects in bulk Cu as a function of Bi atomic % concentration, *x*. **Figure 3** shows the point defect formation energy as a function of Bi content for several types of Bi defects in the Cu lattice (either substitutional or interstitial). Varying Bi doping levels were simulated by inserting Bi defects into differently sized cubic Cu supercells (n × n × n times the unit cell). The defect formation energy was

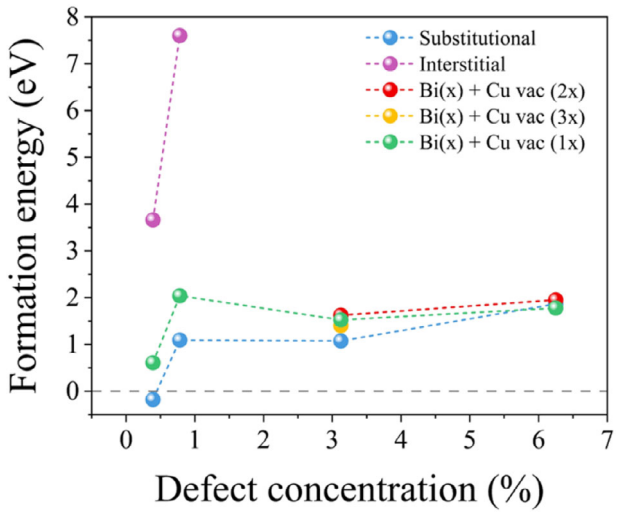

Figure 3. DFT calculated formation energies for substitutional Bi (blue), interstitial Bi (magenta), as well as the Bi substitution + Cu vacancy complexes (in green, red and yellow) as a function of Bi concentration in atomic %. The Cu vacancy concentration corresponds to a multiplication factor ×1 (green dots), ×2 (red dots), or ×3 (yellow dots) times the Bi concentrations. The zero energy reference, marked with a dashed line, is the summation of the atom energy density times the number of atoms in their respective bulk form (fcc Cu and rhombohedral Bi).

calculated by subtracting to the total energy of the Cu-Bi system the total energy of an equal number of atoms in the parent Cu fcc bulk and Bi rhombohedral bulk phases. Thus, negative net values of the formation energy would point toward a stable Cu-Bi alloy. For validation purposes, many configurations were explored (including a few defects per supercell with different defect coordination), aiming to a stability description per defect type and concentration. Our calculations show that interstitial configurations appear quite unlikely, due to the high positive formation energy required being close to 4 eV for low Bi concentrations (<1%) and much larger, in the 8 eV range, for high concentrations. This result is consistent with our previous pair distribution function analysis of X-ray total scattering data in Bi-doped Cu nanowires, where the presence of interatomic correlations indicative of interstitial Bi in the Cu lattice was not detected. Rather, we observed incorporation of substitutional Bi, with indications of local Bi order avoiding nearest neighbor positions.[24] In fact, substitutional configurations are more energetically favorable, with formation energy values between 1 and 2 eV for Bi concentrations up to 6%, (which increase for higher substitutional Bi doping levels). Interestingly, negative formation energies are obtained for Bi concentrations <0.5%. While these quantitative values must be taken with caution (DFT energetics depend quantitatively on the employed exchange-correlation functional), these calculations suggest that low levels of Bi substitution can be in fact stabilized in equilibrium. In any case, and since the growth process of electrodeposition takes place intrinsically out of equilibrium, high amounts of substitutional Bi impurities can be expected even when they exhibit positive formation energies (in the order of an eV). Such impurities would tend to get annealed out of solution if any thermal energy is provided to the system and the impurities are allowed to migrate. This idea is consistent with our experimental findings regarding the initial stabilization of large Bi contents, in the 7% range in as-grown pristine samples, but only low amounts of Bi remaining intra-grain after annealing, as shown in Figure 2.

For the sake of completeness, other defects complexes including Cu vacancies near the Bi dopant were also examined, such as Cu vacancies, which might help stabilize large Bi doping levels since they would contribute to leverage the local charge neutrality when a Bi atom is inserted into a Cu lattice site. DFT shows that the Bi + Cu vacancy complex is less stable than the Bi defect alone by 0.5–1.0 eV for low concentrations. However, at higher concentrations (above 3%) the complex stabilization is enhanced, being the trend reversed at Bi concentration above $x = 6\%$. These calculations suggest that high Bi doping can be achieved at the expense of introducing other point defects in the system. However, caution must be exerted not to over interpret these calculations. The points at $x = 3\%$ and 6% correspond to calculations based on supercell sizes of $2 \times 2 \times 2$ times the unit cell with 1 and 2 Bi atoms, respectively. For multiple defects (either Bi atoms or Cu vacancies) their mutual coordination influences the final total energy value and, therefore, the stability. As the number of defects increases, so does their possible coordination. Therefore, a complete in-depth study would require a thorough study of different possible configurations, which is beyond the scope of this paper. In any case, multiple cases have been explored here, and only the most stable configurations are represented in Figure 3. Nevertheless, these calculations provide a valid context to understand our experimental results, since they point to a finite feasibility to obtain out-of-equilibrium defect complexes consisting of a Cu vacancy near a Bi dopant, which corresponds to a configuration with an increased supercell volume. Both the annealing of Cu vacancies and the migration of Bi out of solution would contribute to promoting the densification of the Cu lattice observed at high temperatures, with small amounts of Bi remaining stable in solution, which is consistent with the experimental data after annealing.

So far, we have shown that annealing temperatures of a few hundred degrees promote an annealing of the Cu lattice along with a densification associated with the annealing of point defects, with small Bi amounts staying within the NW Cu cores. However, the question remains open as for where do the majority of thermally excited Bi atoms go. Low magnification EELS compositional maps of in situ annealed NWs with the nominal 7% Bi doping were compared to pristine samples in order to investigate this issue, as depicted in **Figure 4**. For this study, the specimens were heated again from RT to 400 °C at a rate of 3 °C s^{-1}, held at that temperature for 15 min, and subsequently quenched at the same rate. All maps and images shown in Figure 4 have been acquired at RT, after temperature stabilization. The elemental maps derived from the integrated signal from the Cu $L_{2,3}$ (red) and Bi $M_{4,5}$ (green) edges are shown, for different sets of 7% doped samples with small crystal size -, that is, polycrystalline wires - and large crystal sizes of the order of a micron or more, such as the ones shown before. Polycrystalline NWs shown in Figure 4a present a high amount of grain boundaries (GB). In this case, Cu and Bi maps of pristine materials exhibit a homogeneous Bi and Cu distribution along the wire axis. After treatment at 400 °C, these GBs act as segregation sites for Bi impurities, thanks to the availability of space in the dislocation cores at GBs, phenomenon

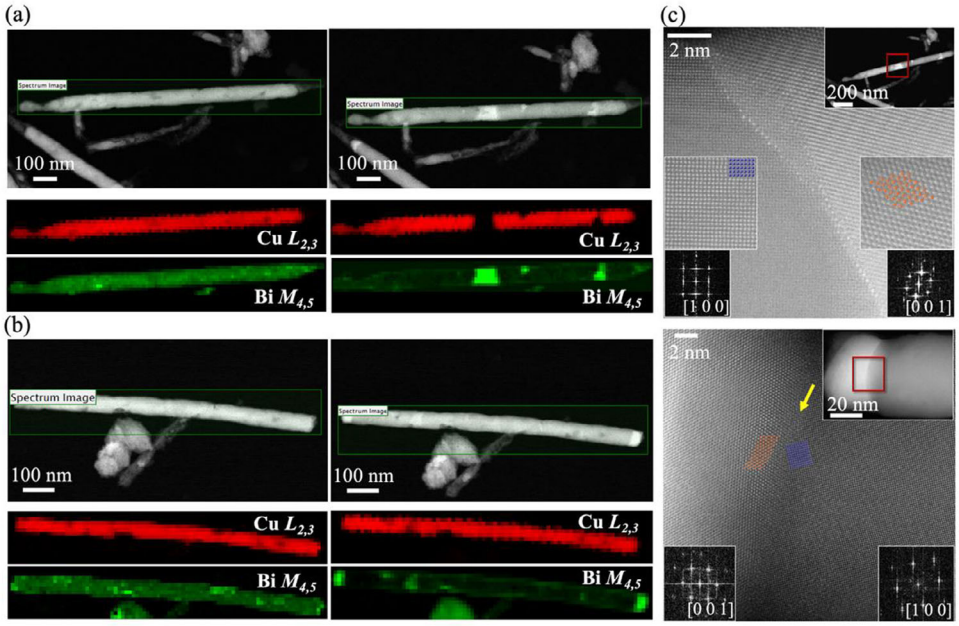

Figure 4. a,b) Low magnification ADF images and simultaneous EELS elemental maps (in false color) for comparison before (left) and after (right) heating of Cu $L_{2,3}$ and Bi $M_{4,5}$ in red and green, respectively, for polycrystalline NW (a) and for large crystal (b) NW. c) Atomic resolution HAADF-STEM images of: (top) a GB within a polycrystalline NW after annealing. The top inset exhibits the low magnification image of the NW, with a red rectangle marking the region where the atomic resolution image was obtained. A yellow arrow points at the Bi/Cu interface. (Bottom) the Bi/Cu interface at the tip of an annealed larger crystal NW (bottom). The inset depicts a low magnification image of the tip, with a red rectangle marking the area where the high magnification image was taken. Fast Fourier transforms showing the relation of relative crystal orientations for every phase are included as lower insets for both samples.

that has already been reported in bulk Cu alloys.[32] A clear enrichment of Bi at these defects is observed, in the form of 100% Bi precipitates along the wire axis (Figure 4a, right panels). A small amount of Bi still remains in solution along the main core of the wire. Similar chemical homogeneity is observed in pristine NWs with larger crystal size, depicted in Figure 4b, where again pre- and post- annealing Bi and Cu maps of a micron long wire are shown. For these NW with larger crystal sizes, and no major amounts of GBs, Bi segregation mainly occurs toward any free surfaces present, which are mostly found at the highly defective NW tips (which serve as growth fronts during synthesis, Figure 4b). While the tips also exhibit a certain degree of oxidation, coverage is not total and nucleation sites for ordered Bi structures are available. In fact, 100% Bi precipitates are observed in both ADF and EELS images at the NW ends. On the other hand, NW lateral surfaces appear fully coated with native Cu and Bi oxides, probably resulting from continuous contact with the porous template during growth. No major annealing induced Bi segregation is observed on those side surfaces.

Such thermally induced Bi precipitates growth steadily with time, and they are crystalline as well – be it when they nucleate in GBs or at the sample tips, as deduced from the images in Figure 4c. The top panel exhibits a high resolution image of a grain boundary after annealing. The upper inset exhibits a low magnification HAADF view of the intra-wire Bi grain, where the high resolution study was carried out. Single, heavy Bi impurities are detected thanks to their brighter contrast sitting within dislocation cores in an evenly spaced fashion. Bi atoms form decorations seemingly placed along a <110>-like direction at the interface of the GBs. They act as nucleation sites for the coherent growth of rhombohedral Bi nanocrystals (right side of the image) which are coherent with the neighboring Cu phase (on the left side of the image). The lower insets show magnified views of the Cu (left) and the Bi (right) lattices, along with overlayed sketches of the crystal structure. Analysis of the images, along with indexing of the diffractograms – fast Fourier transforms (FFTs) in the lower insets – permit establishing a Cu [100]// Bi[001] approximate relationship of orientations between the Cu fcc *Fm-3m* [100] and the Bi precipitate, with a structure compatible with metallic Bi within the rhombohedral *R-3m* space group [001]. This semicoherent interface stabilization is only possible if the Bi segregation takes place in an ordered and steady fashion after nucleation of the single Bi impurities at the arrays of dislocation cores in GBs.

Regarding NWs with larger grain sizes (in the micron range), no major amounts of extended 2D defects such as GBs are present. Since the wires are coated with a layer of native oxide, Bi migration and segregation out of solution takes place mostly toward the free tip ends. Figure 4d shows an atomic resolution view of an interface close to the tip (as shown in the inset, from the region marked with a red square). The image was also acquired at RT after stabilization of the temperature post-quenching. Again, both the Cu and the Bi crystal structures are clearly observed, coherently aligned with each other. The FFT of the bright Bi precipitate at the left end of the tip is shown as an inset. It corresponds to pure Bi, and gives proof again of the formation of metallic Bi in the rhombohedral *R-3m* space group, again aligned down the [001] zone axis. The right area still displays the Cu fcc crystal

lattice oriented in [100] zone axis, as inferred from the FFT in the inset, representing the remainder of the NW, the orientation relationship is again of the type Cu [100]// Bi[001]. Since the relative Bi/Cu grain orientations are the same as in the previous GB case, it can be assumed that this interfacial alignment is particularly stable in the system.

In order to get further insights into the atomistic mechanisms underlying pure Bi precipitate crystallization, further attention was paid to the early stages of Bi nanocrystal segregation on the NW tip surfaces. **Figure 5** shows a set of atomic resolution HAADF images from free surfaces of a nominal 7% Bi doped NW after in situ annealing at 400 °C. Significant faceting along the low index surfaces was detected in high magnification images, as depicted in Figure 5a. This result is to be expected since such surfaces exhibit a lower amount of unfulfilled bonds and, therefore, lower formation energies, so surface faceting typically occurs to minimize the system energy, exposing the more densely packed atomic planes.[33] The annealing induces significant segregation of ordered arrays of Bi atoms, observed in the Z-contrast images as brighter atomic columns are on the NW surface facetted terraces. A "ripple"-like recrystallization is observed on these surfaces, where single Bi atoms are placed over short terraces seemingly intercalating <100> and <110> directions (and the related crystallographic planes) on the NW free ends. Such a self-organized arrangement of dopant atoms on nanoscale facets has been observed before in semiconductors – for example, Bi deposition on GaAs NWs leads to the formation of ordered 1D GaBi atomic chains and 2D islands on the nanowire sidewall facets.[34] However, we are not aware of any evidence of similar phenomena in metallic nanosystems such as these.

In order to gain more information into the 3D geometry and morphology of such atomic structures, 3D depth slicing imaging was attempted by means of acquiring through-focus image series on the tip surfaces. Thanks to the finite depth of field in the aberration corrected STEM, the electron probe can be focused at different depths along the optical axis within the sample, and obtain series of images[35,36] sensitive to the 3D structure of the nanomaterial, including the Bi decorations around the NW free tip. Figure 5b–d shows such a sequence of HAADF atomic resolution images acquired at increasing defocus steps (Δf) of 14 nm. For each panel, the schematics on the lower left corners depict the process of the probe being focused on features sitting at different heights within the material. Our through-focus series shows atomically sharp Bi decorations on all images. They are located on top of the surface terraces, so their contour can be traced in a 3D fashion down the material surface contour. They all exhibit portions of surface Bi planes coming into focus and then getting smeared out to end up disappearing when defocus is increased, allowing other structures to become visible. This way, the surface shape can be monitored, and a 2D continuous surface coating of Bi atoms one atomic plane thick can be imaged on the faceted surface. This monoatomic thick layer of Bi decorations extends over the lateral length scales probed, of the order of tens of nm, and therefore is quite stable (and may act as well as nucleation site for further Bi segregation of coherent nanocrystals). On a first inspection, it appears that these Bi atoms sit preferentially on terrace planes containing the <110> direction. However, a careful inspection of the high resolution images suggests that the atomistic arrangement is not that simple.

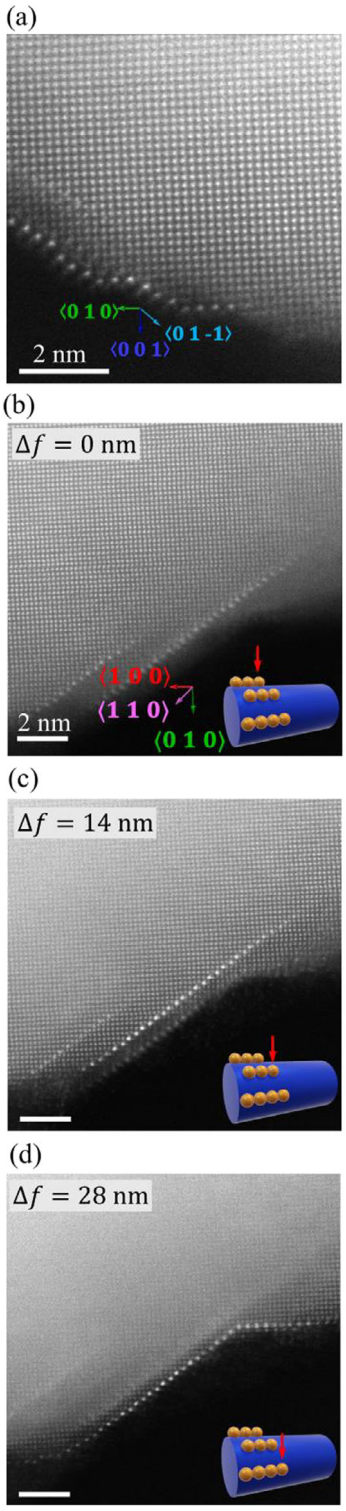

Figure 5. Atomic resolution HAADF-STEM images of an annealed, nominal 7% Bi doped Cu NW, including a through focus series. a) Surface of the NW showing Bi segregation after recrystallisation giving rise to local faceting, with predominant low index atomic planes. b–d) Through focus series acquired at the surface of a NW, with images acquired at relative defocus steps of Δf = 14 nm. The sketches in the lower right summarize how the probe can be focused at different heights within the sample and give rise to a depth slicing- like image series.

Figure 6a shows a magnified portion of the high resolution image of the surface terrace in Figure 5d. A close inspection allows realizing that the Bi monoatomic surface decoration plane is not quite sitting parallel to the square diagonal {110} plane. Instead, a slight deviation is observed along with a ripple and a dimerization in the Bi-Bi distances, with a ...-long-short-long-short-... distribution of nearest neighbor distances along the surface plane. Such distances can be quantified from the images, so Figure 6b exhibits a histogram of the extracted values, with a bin size of 0.05 Å, which is an estimation of the accuracy of such direct measurements on these experimental images. Even with the limited lateral statistics, the data can be fitted to the superposition of two Gaussian curves (plotted in blue and magenta). Their respective centers point toward a bimodal distribution of lattice parameters, of 3.25 ±0.15 Å and 3.81 ± 0.12 Å, for short and long distances respectively. This is the first quantitative hint that the atoms are not evenly spaced as it would be expected from an alignment along a low index {110} plane. Therefore, the most stable atomic surface configuration when Bi segregates out of solution must be a different one. A simple approach based on counting atomic columns gives the impression that the surface orientation may be closer to a {320} or even a {530} higher index plane, which is surprising for a fcc metal such as Cu.

In order to understand the underlying atomic explanation DFT calculations were carried out, considering several surface orientations including the {111}, since it is the most stable terminating plane in pure single element fcc lattices. Bi atoms were added to the surface with increasing concentrations to mimic higher coverages and the resulting surface energy was calculated by taking into account unfulfilled atomic bonds versus bond saturated with Bi atoms. Figure 6c shows the formation energy as a function of Bi coverage for several surface orientations. For surface coverages below 67%, Bi atoms are stable on the (111) surface (green dots). However, for increasing coverages the formation energy becomes positive rapidly, since the large Bi atoms start being too close to each other, preventing a full coverage. This finding explains why this type of Bi / Cu interface is not found in annealed materials. On the other hand, the (530) (blue dots) and (320) (red dots) planes identified in Figure 6a give rise to a very different picture, with negative (stable) energy configurations for coverages up to 100% of the surface area. The schematic on Figure 6a depicts this crystal structure projected along the in-plane projection for a few Bi pairs (Cu atoms in blue, Bi atoms in grey). Two Bi-Bi coordination patterns are observed experimentally, involving different combinations of either nearest neighbors (NN) or next-nearest-neighbors (NNN) distances within the pure Cu structure. For the predominant configuration observed, Bi-Bi coordination distances resemble a dimer-like NNN-NN distance pattern related to 4.0 - 2.6 Å ideal distances, as would be expected from successive atomic jumps along the -<210>-<110>- directions in the Cu fcc structure, resulting into an average <320> direction. According to the calculations in Figure 6c, this is a stable configuration that can give rise to a complete, 100% Bi surface coverage. On occasion other arrangements are also seen. For example, at the right end of Figure 6a the Bi-Bi coordination corresponds more to a NNN-NNN-NN pattern, in this case close to 4.0 - 4.0 - 2.6 Å ideal distances, linked to successive atomic jumps along the <210>-<210>-<110> directions in the fcc structure, which in this case would average into a macroscopic <530> - like structure. After

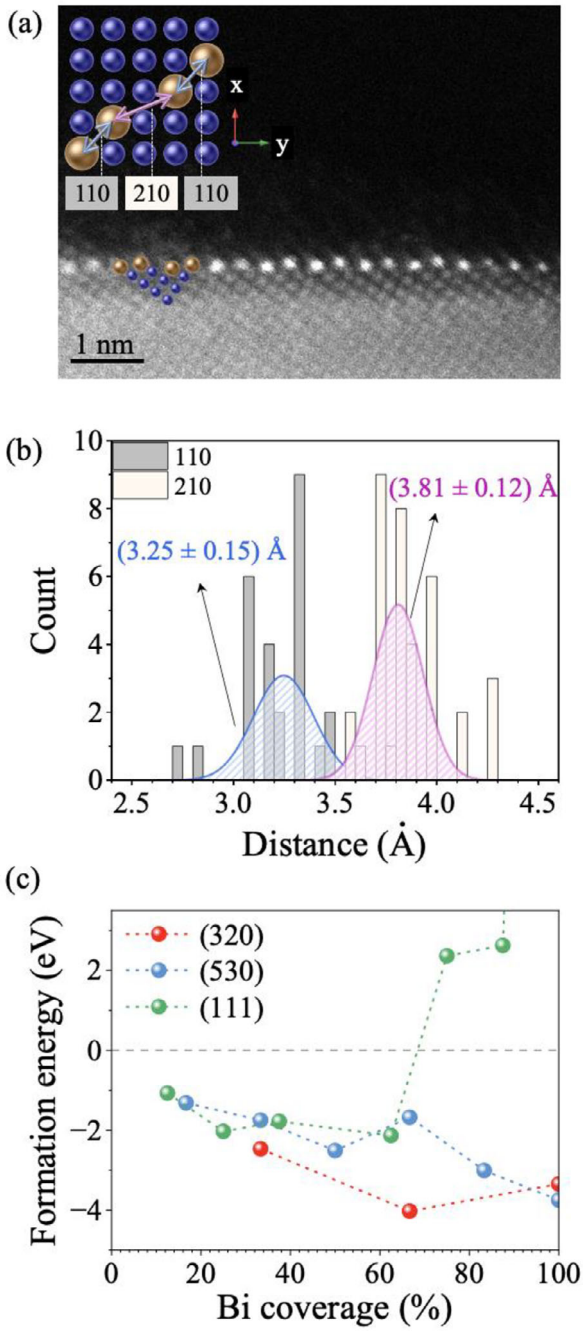

Figure 6. a) HAADF-STEM image showing the Bi dimerization along the {320} plane, magnified from Figure 5d. The inset shows the schematic representation of the top view of the terrace, exhibiting the fcc Cu cell along with the Bi atoms distribution along a short dimer (<110>) and a long dimer (<210>) direction. b) Histogram of the distribution of interatomic distances for short and long Bi dimers, measured from through-focus STEM images. The distributions were fitted with Gaussian functions to extract characteristic dimer distances, and the associated errors were obtained from the standard deviations of the fits. c) Surface formation energy (eV) as a function of the Bi coverage (in %). The formation energy (FE) as referenced to the Cu surface energy for specific orientation planes and the total energy of the bulk Bi rhombohedral phase (FE equals the total energy of the doped surface minus the total energy of un-doped surface minus the total energy of Bi atoms).

allowing the DFT calculations to relax, these distances result into 3.82–3.28 Å or 3.82–3.82–3.28 Å interatomic distance patterns, which help to stabilize and accommodate the Bi cations on the Cu lattice. STEM images also show other local arrangements, such as Bi atoms arranged down the <001> direction. Combining this direction with the previously shown, the calculations show how a complete 2D lateral coverage of Bi can be achieved on those {320} and {530} families of atomic planes.

With these calculations in mind, we can conclude that after surface Bi segregation starts, for low Bi coverage the most stable configuration, relative to the specific surface energy, corresponds to the {111} family of planes. This is to be expected as it is the most stable case for pure Cu termination and will remain like that till Bi-Bi interaction becomes sizeable. This is the case at a small 33% Bi coverage since one in-plane Bi-Bi direction is <110>, that of the NN distance. Above 33% coverage the most stable configuration becomes a {320}-like plane until just before the full coverage when it becomes less stable than the {530} plane. This last transition can be understood from the perspective that the two directions discussed in Figure 6a, <320> and <530>, are constituted by linear combinations of <110> and <210> directions (as well as to <001>) corresponding to the NN and NNN distances, respectively. <110> direction maximizes the Bi defect concentration while <210> show a compromise between a moderate Bi concentration and larger Bi-Bi distances than those Cu-Cu NN distances necessary to accommodate the large Bi atoms at dense coverage concentration.

These theoretical findings are consistent with the experimental measurements. The histogram of direction-dependent distances is presented in Figure 6b, appears sensitive to the presence of both short-distance <110> and long-distance <210> orientations. For the <110> direction, the normal distribution of measured distances revealed a Gaussian component, shown in blue, with a mean value of 3.3(2) Å (blue). This value closely matches the values predicted by DFT calculations, suggesting its physical origin is well captured by theory. In the <210> direction, a single Gaussian distribution is observed, centered at 3.8(1) Å (magenta curve). This value is also in qualitative agreement with DFT, validating the theoretical model discussions. These results show that for such surface orientation, the nucleation of a Bi monoatomic layer is stable over long lateral distances. Furthermore, it very likely represents the onset of nucleation for the coherent Bi grains that appear on the NW tips, as shown in Figure 4c (bottom panel).

3. Discussion

Our results show that heating induced Bi segregation reduces the Bi concentration in the system down to levels of the order of 1–2%, which are fully stable. This finding is promising for spintronic applications, since a giant SHE would still be possible for these doping levels. Therefore, Cu-Bi nanosystems with large average crystal sizes and Bi doping levels in such low range can be proposed as building blocks for future spintronic devices for spin-charge conversion. In addition to the potential applications of Bi-doped materials in spintronics, magnetic nanowires are the building blocks of data storage, logic, and neuromorphic devices.[37–39] In this context, the inherent limitations of areal density in 2D systems have fueled interest in advancing into the third dimension,[40] a field in which electrodeposited magnetic nanowires are excellent playground for exploring 3D and curvilinear effects in finite-size systems.[41–43] In all these applications, information is based in current control of magnetic domain walls dynamics. Therefore, the study of Joule effect in these nanowires under operando conditions, similar to the one reported in this manuscript, is key for further development of real devices.

A very different finding, potentially compromising performance, regards higher doping levels where thermal energy gives rise to relevant Bi migration. Seminal studies of fractures in Cu-Bi alloys that have undergone heating treatments,[44] showed that faceting is most likely to occur when there is a significant size difference between matrix and impurity atoms, as is our Cu-Bi solution.[44] In fact, faceting is linked to the thermally induced segregation of Bi at GBs, which leads to embrittlement. According to some early reports in metallurgy, the Cu-Bi alloy system is characterized by an extremely low solubility of Bi in Cu, with the solid solubility reported to be less than 0.01% at 800 °C. This system is primarily classified as a eutectic type, with the eutectic temperature of ≈270 °C, occurring close to the one of pure Bi.[45] Below this temperature, the alloy solidifies into different solid phases, even though the individual metals may remain liquid at higher temperatures. Above the eutectic temperature, particularly ≈300 °C, our data suggest that the Cu-Bi system enters a phase where Cu and Bi species begin to separate due to their mutual insolubility, with no stable intermetallic phases, so the observed segregation into inhomogeneous Cu-rich and Bi-rich regions is consistent with previous knowledge.[45] As we also found, previous reports show that at temperatures above 400 °C Bi solubility into Cu is reduced. The question remains whether such previous bulk studies can be extrapolated to nanometric length scales, where the atomic behavior and miscibility may significantly differ from those observed in bulk materials, due to a higher surface-to-volume ratio, quantum effects, altered grain boundary behavior, size-dependent mechanical properties, and changes in thermal, optical, and magnetic characteristics. One way or the other, our findings show that NWs with high Bi doping levels can still be proposed as constituents of future devices as long as the operation temperatures can be kept below the 200 °C range.

4. Conclusions

Advanced electron probes combined with first principles calculations have been employed to study the response of highly doped (7% Bi) Cu NWs to temperatures up to 400 °C. Atomic resolution STEM imaging shows that pristine NWs, synthetized by room temperature electrodeposition, exhibit a high degree of crystallinity with average grain sizes that can span into the micron range. Compositional EELS mapping confirms that Bi species in as-grown materials are homogeneously distributed within the NW cores. DFT calculations show that Bi is unlikely to occupy interstitial sites due to high formation energies (> 4 eV). In substitutional positions, however, formation energies ≈1 eV are obtained for Bi concentrations above 1%, pointing to a likely, metastable Bi substitution. On the other hand, for concentrations below 1%, negative formation energies ≈−0.2 eV are found, pointing toward full Bi stability within the Cu fcc lattice for such low concentrations. In situ HAADF imaging shows that

the thermal energy transferred to the system by the Joule effect due to electric current injection triggers significant mass segregation phenomena at the nanoscale. First, metastable Bi is forced to segregate out of solution to form nanoclusters and, eventually, the whole Cu wire melts. Temperature controlled in situ annealing processes were carried out to reproduce such processes in a controlled fashion. A clear onset for noticeable structural changes was detected when temperatures in the 250 °C range were reached, which is close to the melting temperature of pure Bi. For treatments at slightly higher temperatures of 400 °C, the Cu lattice gets annealed, leading to a denser NW core with an ≈1% reduction of lattice parameters thanks to the segregation of Bi atoms or other defects, such as Cu vacancies. Migration of excess Bi takes place toward grain boundaries or to any free surfaces at the NW tips. At the early stages, monoatomic thick Bi decorations can be identified at these extended defects. These occur preferentially along {320} (and also at {530}) atomic planes with a dimerization of the Bi decorations, leading to a stable Bi coverage over long lateral length scales. Further Bi segregation gives rise to the growth of Bi nanoprecipitates exhibiting the bulk rhombohedral space group (*R-3m*), with a predominant common orientation relationship of the type Cu [100]// Bi[001]. After annealing and quenching the samples back to room temperature, low Bi intra-grain contents in the 1–2% range are still detected by EELS, consistent with the theoretical calculations showing the feasibility of achieving a stable low Bi doping, thermodynamically favorable even after thermal activation. This is a most promising result, since such Bi doping levels can still give rise to a significant SHE and, thus, promote this system as potential building block of future spintronic applications.

5. Experimental Section

Synthesis of $Cu_{93}Bi_7$ Nanowires: $Cu_{93}Bi_7$ – 7% atomic percent Bi doping - NWs were synthesized by template-assisted electrochemical deposition in the pores of anodized aluminum oxide (AAO) templates using the growth conditions described in our previous work.[24] To prepare the electrolyte $Bi(NO_3)_3$ (8 mM), $CuSO_4$ (40 mM) and KNO_3 (1.15 M) were mixed in a mixture of deionized water and glycerol (10% in vol.), together with two different amounts of tartaric acid ($C_4H_6O_6$) (0.33 M and 1 M). HNO_3 was added until the solution became transparent (pH∼ 0.9). The two concentrations of tartaric acid lead to different types of NWs with different average crystallite sizes between 200 nm and 1 µm.

Electron Microscopy & Spectroscopy: STEM-EELS characterization was carried out using a JEOL JEM-ARM200cF aberration corrected electron microscope operated at 200 kV, equipped with a cold field emission gun and a Gatan Quantum EEL spectrometer. For the imaging conditions used, the probe size, and thus spatial resolution, is ≈0.7 Å. Random noise was removed from EEL spectra using principal-component analysis.[46] Prior to quantification, the background was removed using a power law fit before integration of the signal in order to produce EELS maps. For in situ biasing or heating studies, the NWs (stored in an ethanol solution) were drop-casted onto Wildfire+Lightning micro-electro-mechanical system (MEMS) nano-chips with SiN_x membranes and Wildfire MEMS nano-chips compatible with the DENSsolutions Lightning D9+ double-tilt holder used for this work. In order to improve the statistics of this study, first a low magnification analysis of every sample was carried out to check the material homogeneity over lateral length scales of the order of tens of microns, including the inspection of tens of nanowires. Statistically representative NWs were selected then for high resolution analysis within each sample. Data from at least ten different materials were obtained this way, and found to be consistent with previous works,[22–24] before attempting in situ measurements.

First-Principles Calculations: Density-functional theory (DFT) calculations have been performed using the projector augmented wave method.[47–50] The density functionals adopted for the electronic exchange and correlation terms correspond to the generalized gradient approximation, as conceived by Perdew-Burke-Ernzerhof.[51] We modelled the energetic and electronic properties of Bi-doped Cu configurations by either including the Bi atoms as substitution or interstitial to the Cu structure characterized by a one atom basis and a fcc lattice. Most of the stability curves as a function of the Bi concentration were calculated as a single substitution to one Cu atom in increasingly larger lattices so the concentration can be varied accordingly to the number of atoms contained in the (super-)cell. A similar approach was followed for the Cu vacancy + Bi complex concentration. When multiple defects (either Bi atoms and/or Cu-vacancies) were calculated, several configurations were considered in a non-exhaustive approach in order to get an understanding of the most stable case as a function of the defect concentration.

An example of the (minimum) concentration determination in a 4 × 4 × 4 times the unit cell (uc) is: $\frac{1\ Bi}{4x4x4uc\ \frac{4Cu}{uc}} = 0.004 = 0.4$ Bi%. The calculations were performed using a plane wave energy cutoff of 370 eV, including spin polarization and a k-point mesh of 12 × 12 × 12 for the Cu unit cell, which is generated by Monkhorst-Pack scheme.[52] K-points mesh was adapted for different supercell sizes so that the linear density of points was the same to that of the uc calculation. For convergence validation purposes larger bulk Cu calculations with denser meshes of up to 20 × 20 × 20 and higher energy cutoffs of up to 500 eV were performed, obtaining energy differences within the chemical accuracy of 1 meV $atom^{-1}$. Full parameter relaxation was allowed for the structural (lattice and atom position) and electronic configuration obtaining the resulting properties when the Hellman-Feynman forces on each atom becomes less than 0.01 eV $Å^{-1}$.

Statistical Analysis: Quantitative treatment of STEM images was carried out in the Gatan GMS Digital Micrograph suite. Distributions of lattice spacings were measured from HAADF intensity profiles by using scripts to locate the centers of mass (CoM) of atomic columns. Then intercolumn distances were computed between adjacent CoM positions. Values given here correspond to the mean calculated over 8–12 equivalent column pairs, and the experimental uncertainty is estimated as approximately twice the value of the resulting standard deviation (which is of ≈0.02 Å).

Supporting Information

Supporting Information is available from the Wiley Online Library or from the author.

Acknowledgements

Financial support from Ministerio de Ciencia, Innovación y Universidades of Spain via grants # PID2021-122980OB-C51, PID2021-122980OB-C52, TED2021-129254B-C21, SpinRed2 RED2022-134649-T and from Comunidad de Madrid via grants MAD2D-UCM3 and TEC-2024/TEC-380 (Mag4TIC-CM) is acknowledged. Fruitful discussions with Marta D. Rossell on monoatomic Bi decorations are acknowledged. Electron microscopy observations carried out at Centro Nacional de Microscopía Electrónica, ICTS ELECMI, Madrid (Spain). This project has received funding from the European Union under the Horizon Europe Marie SkłodowskaCurie Actions under project No. 101109595 (MAGWIRE).

Conflict of Interest

The authors declare no conflict of interest.

Data Availability Statement

The data that support the findings of this study are available from the corresponding author upon reasonable request.

Keywords

electron energy-loss spectroscopy, in situ characterization, nanosystems, scanning transmission electron microscopy, spintronics

Received: July 15, 2025
Revised: November 14, 2025
Published online:

[1] I. Zutic, J. Fabian, S. D. Sarma, *Rev. Mod. Phys.* **2004**, *76*, 323.
[2] D. C. Ralph, M. D. Stiles, *J. Magn. Magn. Mater.* **2008**, *320*, 1190.
[3] J. Sinova, S. O. Valenzuela, J. Wunderlich, C. H. Back, T. Jungwirth, *Rev. Mod. Phys.* **2015**, *87*, 1213.
[4] B. L. Zink, *J. Magn. Magn. Mater.* **2022**, *564*, 170120.
[5] K. I. Uchida, R. Iguchi, *J. Phys. Soc. Jpn.* **2021**, *90*, 122001.
[6] R. Guedas, V. Raposo, J. L. Prieto, *J. Appl. Phys.* **2021**, *130*, 191101.
[7] S. R. Boona, R. C. Myers, J. P. Heremans, *Energy Environ. Sci.* **2014**, *7*, 885.
[8] S. A. Razavi, D. Wu, G. Yu, Y.-C. Lau, K. L. Wong, W. Zhu, C. He, Z. Zhang, J. M. D. Coey, P. Stamenov, P. Khalili Amiri, K. L. Wang, *Phys. Rev. Appl.* **2017**, *7*, 024023.
[9] A. Guedeja-Marrón, F. Ajejas, A. Gudin, I. Arnay, L. Perez, P. Perna, M. Varela, *Phys. Rev. Mater.* **2025**, *9*, 064411.
[10] J. Romero, H. Prima-Garcia, M. Varela, S. G. Miralles, V. Oestreicher, G. Abellán, E. Coronado, *Adv. Mater.* **2019**, *31*, 1900189.
[11] M. L. Bols, J. Ma, F. Rammal, D. Plessers, X. Wu, S. Navarro-Jaén, A. J. Heyer, B. F. Sels, E. I. Solomon, R. A. Schoonheydt, *Chem. Rev.* **2024**, *124*, 2352.
[12] B. G. Mullens, M. Saura-Múzquiz, G. Cordaro, F. P. Marlton, H. E. Maynard-Casely, Z. Zhang, G. Baldinozzi, B. J. Kennedy, *Chem. Mater.* **2024**, *36*, 5002.
[13] J. Romero, M. Varela, M. Assebban, V. Oestreicher, A. Guedeja-Marrón, J. L. Jordá, G. Abellán, E. Coronado, *Chem. Sci.* **2020**, *11*, 7626.
[14] A. Ziegler, H. Graafsma, X. F. Zhang, J. W. M. Frenken, *In-situ Materials Characterization: Across Spatial and Temporal Scales*, Springer, Berlin**2014**.
[15] M. T. McDowell, K. L. Jungjohann, U. Celano, *Nano Lett.* **2018**, *18*, 657.
[16] E. Adabifiroozjaei, E. Rastkerdar, Y. Nemoto, Y. Nakayama, Y. Nishimiya, M. Fronzi, Y. Yao, M. T. Nguyen, L. Molina-Luna, T. S. Suzuki, *J. Mater. Sci.* **2023**, *58*, 2456.
[17] L. Zeng, C. Gammer, B. Ozdol, T. Nordqvist, J. Nygård, P. Krogstrup, A. M. Minor, W. Jäger, E. Olsson, *Nano Lett.* **2018**, *18*, 4949.
[18] F. M. Ross, *Science* **2015**, *350*, aaa9886.
[19] M. Perxés Perich, J.-W. Lankman, C. J. Keijzer, J. E. S. van der Hoeven, *Nano Lett.* **2025**, *25*, 5444.
[20] G. Ummethala, R. Jada, S. Dutta-Gupta, J. Park, A. H. Tavabi, S. Basak, R. Hooley, H. Sun, H. H. Pérez Garza, R.-A. Eichel, R. E. Dunin-Borkowski, S. R. K. Malladi, *Commun. Chem.* **2025**, *8*, 8.
[21] Y. Niimi, Y. Kawanishi, D. H. Wei, C. Deranlot, H. X. Yang, M. Chshiev, T. Valet, A. Fert, Y. Otani, *Phys. Rev. Lett.* **2012**, *109*, 156602.
[22] S. Ruiz-Gómez, C. Fernández-González, A. Guedeja-Marrón, A. Serrano, M. Á. González Barrio, M. Varela, A. Mascaraque, L. Pérez, *J. Magn. Magn. Mater.* **2022**, *545*, 168645.
[23] S. Ruiz-Gómez, R. Guerrero, M. W. Khaliq, C. Fernández-González, J. Prat, A. Valera, S. Finizio, P. Perna, J. Camarero, *Phys. Rev. X.* **2022**, *12*, 031032.
[24] A. Guedeja-Marrón, H. L. Andersen, G. Sánchez-Santolino, L. Zeng, A. Ranjan, I. García-Manuz, F. Fauth, C. Dejoie, E. Olsson, P. Perna, M. Varela, L. Pérez, M. Saura-Múzquiz, *ACS Nano* **2025**.
[25] R. Hoffmann, D. Weissenberger, J. Hawecker, D. Stöffler, *Appl. Phys. Lett.* **2008**, *93*.
[26] R. Holm, E. Holm, *Electric Contacts: Theory and Application*, Springer, Verlag **1967**, p. 9780387038759.
[27] H. H. P. Garza, Y. Pivak, L. M. Luna, et al., in 19th International Conference on Solid-State Sensors, Actuators and Microsystems (Transducers), **2017**: 2155-2158.
[28] F. Ebrahimi, Q. Zhai, D. Kong, *Scr. Mater.* **1998**, *39*, 315.
[29] C. H. Seah, S. Mridha, L. H. Chan, *J. Vac. Sci. Technol., A* **1999**, *17*, 1963.
[30] J. Verbeeck, S. Van Aert, G. Bertoni, *Ultramicroscopy* **2006**, *106*, 976.
[31] J. Verbeeck, S. Van Aert, *Ultramicroscopy* **2004**, *101*, 207.
[32] G. Duscher, M. F. Chisholm, U. Alber, M. Rühle, *Nat. Mater.* **2004**, *3*, 621.
[33] K. K. Chawla, *Composite Materials: Science and Engineering*, Springer, New York **2013**.
[34] Y. Liu, J. V. Knutsson, N. Wilson, E. Young, S. Lehmann, K. A. Dick, C. J. Palmstrøm, A. Mikkelsen, R. Timm, *Nat. Commun.* **2021**, *12*, 5990, https://www.nature.com/articles/s41467-021-26148-4.
[35] S. Wang, A. Y. Borisevich, S. N. Rashkeev, M. V. Glazoff, K. Sohlberg, S. J. Pennycook, S. T. Pantelides, *Nat. Mater.* **2004**, *3*, 143.
[36] K. van Benthem, A. R. Lupini, M. Kim, H. S. Baik, S. Doh, J.-H. Lee, M. P. Oxley, S. D. Findlay, L. J. Allen, J. T. Luck, S. J. Pennycook, *Appl. Phys. Lett.* **2005**, *87*, 034104.
[37] S. Parkin, S. H. Yang, *Nat. Nanotechnol.* **2015**, *10*, 195.
[38] Z. Luo, A. Hrabec, T. P. Dao, G. Sala, S. Finizio, J. Feng, S. Mayr, J. Raabe, P. Gambardella, L. J. Heyderman, *Nature* **2020**, *579*, 214.
[39] S. A. Siddiqui, S. Dutta, A. Tang, L. Liu, C. A. Ross, M. A. Baldo, *Nano Lett.* **2020**, *20*, 1033.
[40] C. Granata, A. Vettoliere, R. Russo, M. Fretto, N. De Leo, V. Lacquaniti, *Appl. Phys. Lett.* **2013**, *103*, 102602.
[41] S. Ruiz-Gómez, C. Abert, P. Morales-Fernández, C. Fernández-González, S. Koraltan, L. Danesi, D. Suess, M. Varela, G. Sánchez-Santolino, N. Bagués, M. Foerster, M. Á. Niño, A. Mandziak, D. Wilgocka-Slezak, P. Nita, M. Koenig, S. Seifert, A. Hierro-Rodriguez, A. Fernández-Pacheco, C. Donnelly, *Nat. Commun.* **2025**, *16*, 7422.
[42] L. Alvaro-Gómez, J. Hurst, S. Hegde, S. Ruiz-Gómez, E. Pereiro, L. Aballe, J. C. Toussaint, L. Pérez, A. Masseboeuf, *Phys. Rev. Res.* **2025**, *7*, 023092.
[43] C. Fernández-González, L. Álvaro-Gómez, L. Fernández-García, P. Morales-Fernández, L. Gómez-Cruz, M. W. Khaliq, C. Donnelly, M. Foerster, M. Á. Niño, E. Pereiro, E. Martínez, M. Jaafar, L. Aballe, L. Pérez, S. Ruiz-Gómez, *Nano Lett.* **2025**, *25*, 10648.
[44] A. M. Donald, L. M. Brown, *Acta Metall.* **1979**, *27*, 59.
[45] D. J. Chakrabarti, D. E. Laughlin, *Bull. Alloy Phase Diagrams* **1984**, *5*, 148.
[46] M. Bosman, M. Watanabe, D. T. L. Alexander, V. J. Keast, *Ultramicroscopy* **2006**, *106*, 1024.
[47] G. Kresse, J. Furthmuller, *Phys. Rev. B* **1996**, *54*, 11169.
[48] G. Kresse, D. Joubert, *Phys. Rev. B* **1999**, *59*, 1758.
[49] G. Kresse, J. Furthmuller, *Comput. Mater. Sci.* **1996**, *6*, 15.
[50] G. Kresse, J. Hafner, *Phys. Rev. B* **1993**, *47*, 558.
[51] J. P. Perdew, K. Burke, M. Ernzerhof, *Phys. Rev. Lett.* **1996**, *77*, 3865.
[52] H. J. Monkhorst, J. D. Pack, *Phys. Rev. B* **1976**, *13*, 5188.